JOURNAL OF APPLIED ELECTROCHEMISTRY 22 (1992) 541–552

Influence of the heat treatment in the electrochemical corrosion of Al–Zn–Mg alloys

P. L. CABOT, F. CENTELLAS, J. A. GARRIDO, R. M. ROGRÍGUEZ, E. BRILLAS, E. PÉREZ

Departament de Química Física, Facultat de Química, Universitat de Barcelona, Av. Diagonal 647, 08020 Barcelona, Spain

A. V. BENEDETTI

Departamento de Fisicoquímica, Instituto de Química, UNESP, Caixa Postal 355, 14.800, Araraquara, SP, Brazil

P. T. A. SUMODJO

Departamento de Química Fundamental, Instituto de Química, USP, Cidade Universitaria, Caixa Postal 20780, CEP 01498, São Paulo, SP, Brazil

Received 12 July 1991; revised 2 October 1991

The localized corrosion of Al–(5.03%)Zn–(1.67%)Mg–(0.23%)Cu alloys and high purity Al has been studied using electrochemical techniques, optical microscopy, SEM and EDX. The samples were previously submitted to different heat treatments in which coherent and incoherent $MgZn_2$ precipitates with different distribution and aggregation degree were produced. The influence of NaCl and Na_2SO_4, dissolved oxygen, immersion time and convection were studied. In NaCl solutions, pitting potentials for the alloys were more negative than for aluminium, indicating an increase in their susceptibility to localized corrosion. Moreover, annealed and cold-rolled alloys presented more negative pitting and repassivation potentials than those submitted to age hardening with direct or interrupted quenching. In annealed and cold-rolled samples, pit nucleation and propagation takes place in the zones where $MgZn_2$ is accumulated. In the case of the age-hardened alloys, a double pitting behaviour is observed, the first one in the magnesium and zinc enriched regions and the second in the matrix. While the cold water quenched alloy is susceptible to stress corrosion cracking, the alloy submitted to the interrupted quenching process is less susceptible to intergranular attack. The sulphate ion shifts the pitting potential of aluminium and the alloys by chloride towards more positive values because it impedes local accumulations of the latter.

1. Introduction

Al–Zn–Mg alloys were studied for the first time in 1913 [1] and their good mechanical properties, after adequate heat treatment, were demonstrated in 1926 [2]. The most interesting properties of these alloys, which lead to structural applications (mainly as constructional materials), are age-hardenability, good corrosion resistance, weldability and low density [3]. Several studies [4–14] have shown that small additions of other elements, particularly Cu, Cr and Zr, improve the properties of Al–Zn–Mg alloys. Cordier *et al.* [15, 16] determined an optimum Zn : Mg ratio of 3 : 1 and a limit of 7% for the total quantity of both elements in order to obtain a weldable Al–Zn–Mg alloy with good stress-corrosion cracking (SCC) resistance. Also, Zn and Mg contents in the range 4.9–5.2% and 1.6–1.8%, respectively, were suggested to assure the minimum strengths required for a high-strength constructional material [16]. Hardenability of the alloys having such compositions is due to the formation of $MgZn_2$ precipitates in the ageing process [4, 15, 16]. According to Cordier *et al.* [8], the addition of 0.15–0.20% Cu to Al–5% Zn–1.7% Mg increases its SCC resistance.

Al–Zn–Mg alloys have been studied from the viewpoints of microstructure, mechanical properties and the usual loading tests of SCC resistance. Galvele and De Micheli [17], Maitra and English [18] and Byrne [19] have shown the utility of electrochemical polarization methods to study the susceptibility to intergranular corrosion and therefore to stress-corrosion cracking (SCC) of Al–4% Cu and Al–6% Zn–2.5% Mg–1.7% Cu–0.2% Cr (known as 7075) alloys. For 7075-T651 and 7075-T7351 [18], two breakdown potentials were identified in the potentiokinetic anodic polarization curves, the first assigned to the Mg and Zn enriched phase in the vicinity of the grain boundaries and the second to the matrix. The decrease of SCC susceptibility by overaging to the T7351 temper was explained by the Cu depletion of the solid solution matrix, which reduced the difference between the pitting potentials of the grain boundaries and the matrix. Byrne demonstrated Cu incorporation into the matrix

0021-891X/92

precipitates using EDX and explained in the same way the increase in SCC resistance of 7075-T73 when submitted to different T7 ages [19].

In the present work, the electrochemical polarization methods, optical microscopy, SEM and EDX are applied to study the relation between microstructure and localized corrosion phenomena of high-strength, weldable and SCC resistant Al–5% Zn–1.7% Mg–0.2% Cu alloy. Different microstructures were obtained using the corresponding heat treatments in order to gain a better understanding of the effect of Cu, Zn and Mg segregation and distribution and size of $MgZn_2$ precipitates. The corroding media comprised solutions of different chloride and sulphate concentrations (simulating atmospheric corrosion conditions). The effect of the presence of dissolved oxygen, immersion time and convection were also examined.

2. Experimental details

2.1. *Preparation of the test samples*

Alloy electrodes were obtained from 5 kg ingots (Kingston Laboratories, Ontario, Canada), which were homogenized at 500° C for 4 h, hot rolled to a thickness of 1 cm and cold rolled to a thickness of 0.4 cm. At this stage, the spectrographic analysis of the alloy gave a content of 5.03% Zn, 1.67% Mg and 0.23% Cu. The Si content was 0.006% and Nb, Ti, Cr, Fe, Ni, V and Mn were less than 0.001%. From these sheets, cylinders of 2.5 mm diameter were obtained and then four test samples, named HST, HA, HB and HC, were prepared following different heat treatment procedures based in the equilibrium phase diagrams of Al–Zn–Mg alloys and on the effect of quenching after solution heat treatment [4, 8, 15, 16, 20, 21]. Sample HST was not submitted to any heat-treatment, still having a 60% of deformation due to the previous rollings. Sample HA was annealed at 480° C for 24 h and then, slowly cooled for 48 h. Sample HB was solution heat treated at 480° C for 1 h, quenched in cold water at 10° C (direct quenching) and naturally aged for 3 days at room temperature, then artificially aged by heating at 90° C for 8 h and subsequently, at 135° C for 24 h. Sample HC was solution heat treated at 480° C for 1 h, rapidly cooled in a salt bath at 400° C for 2 min, quenched in cold water at 10° C (interrupted quenching) and also aged following the same sequence as in the case of the specimen HB. The purpose of these heat treatments was to test the effect of material deformation (HST) and the behaviour of the samples presenting phase equilibria (HA) and those, age-hardened, applicable as constructional materials (HB and HC) [21]. High-purity aluminium (99.9995%) cylinders of 3 mm diameter were also prepared for comparative tests.

2.2. *Electrochemical experiments*

The working electrodes were encapsulated in epoxy resin or, when using the RDE, in a Teflon matrix. All the specimens were mechanically polished up to 1 μm (diamond paste) and cleaned with ethanol in ultrasound bath.

The experiments were conducted in a conventional three-electrode cell at 25.0 $\pm$ 0.1° C. The auxiliary electrode was a platinized Pt wire and the reference, connected via a Luggin capillary, a SCE or a saturated $Hg/Hg_2SO_4/K_2SO_4$ electrode (when the test solution contained sulphate). All potential values given in this paper are referred, unless otherwise indicated, to the SCE.

The cyclic polarization (CP) curves, the Tafel experiments, as well as the corrosion potential (E_{cor}) against time and the polarization resistance (R_P) measurements, were performed by means of a PAR 273 potentiostat commanded by an IBM PS 50Z computer. The influence of forced convection was studied using an RDE supplied by Pine Instruments.

The test solutions were 0.01 and 0.1 M NaCl, 0.1 M Na_2SO_4 and 0.01 M NaCl–1 M Na_2SO_4, saline concentrations simulating atmospheric conditions. All solutions were prepared from analytical reagent (Merck) NaCl and Na_2SO_4 and Millipore Milli-Q quality water. The electrode response in these media was studied after different time of immersion, under aerated and deaerated conditions. Deaeration was performed by argon bubbling for 3 h through a vigorously stirred solution, circulating argon over the electrolyte during the experiments.

2.3. *Microscopic examination*

The surface of the alloys was examined before and after the electrochemical experiments in a Carl Zeiss Metaval metallographic microscope and in a Jeol-JSM 840 SEM. The surface microstructure of specularly polished samples, prior to electrochemical polarization, was revealed using 3A (concentrated) or 3B (diluted) Keller's reagents [22]. The samples to be observed under the SEM, immediately after preparation, were rinsed in ethanol, dried in an argon atmosphere and stored under high vacuum. The microanalysis of the surface was carried out by EDX (Link Systems), under conditions in which the electron penetration depth was estimated to be 1.9 μm.

3. Results

3.1. *Microstructure of the alloys*

SEM observation of the specularly polished samples showed the existence of particles in the grain boundaries of alloys HST and HA. The EDX microanalysis of such particles indicated the presence of Zn and Mg and therefore, were attributed to $MgZn_2$, the typical compound formed in the alloys studied [4, 15, 16]. It must be noticed that Cu was also evidenced in the $MgZn_2$ grain boundary precipitates by EDX microanalysis of spots situated in such regions. These precipitates were small, discontinuous and long shaped,

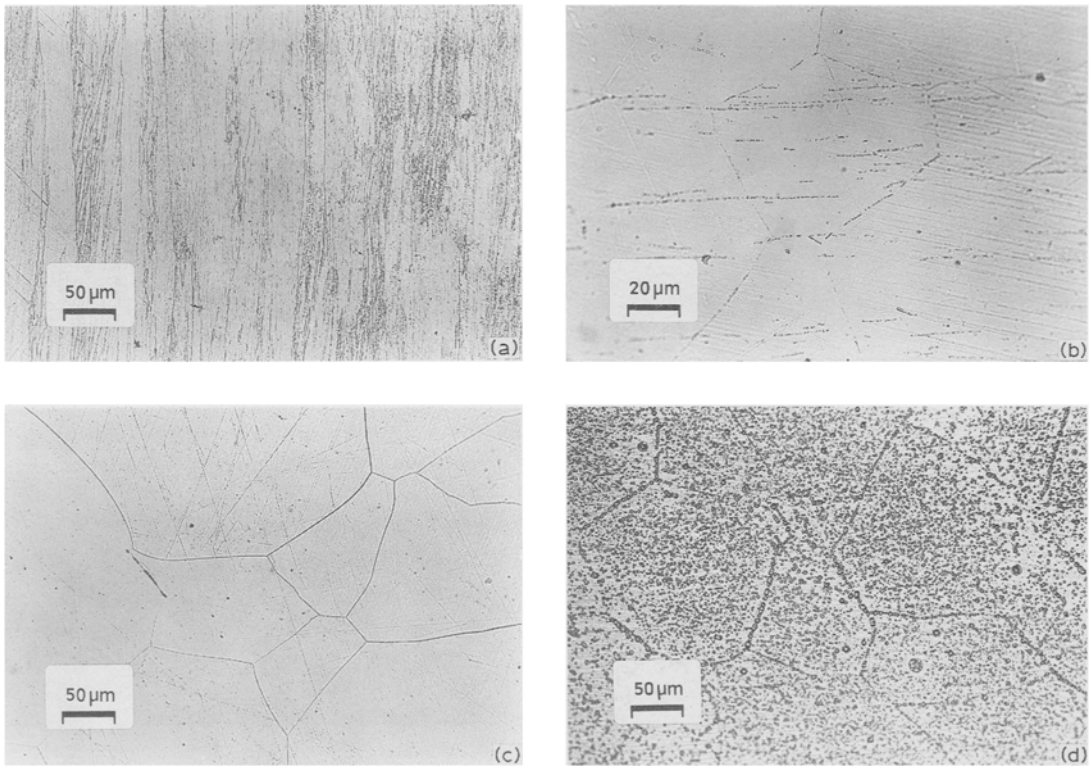

Fig. 1. Results of different Keller's etching of the specularly polished Al–Zn–Mg alloys under study. (a) Alloy HST, 20 s etching in 3A Keller's reagent; (b) alloy HA, 30 s etching in 3B Keller's reagent; (c) alloy HB, 30 s in 3A Keller's reagent and (d) alloy HC etched in 3A Keller's reagent for 8 min.

following the grain boundary direction. Such precipitates in alloy HST were found to be smaller than in the case of alloy HA. For the latter alloy, parallel transgranular bands of very small $MgZn_2$ particles were also observed. Any precipitates in the case of alloys HB and HC could not be detected under the SEM.

X-ray mappings of Zn and Mg resulting from EDX microanalysis were also performed for all the alloys polished up to a mirror finish, using magnifications in the range 200–2000X. Such mappings showed a quite uniform Zn and Mg distribution in the grains even in alloys HST and HA. This is not surprising because of the relative solubility of Zn and Mg in Al, as well as the distribution and the very fine form of the $MgZn_2$ precipitates.

The mean grain size of the alloys HA, HB and HC was determined to be $225 \pm 40\,\mu m$ using standard metallographical methods [21]. To obtain more information on the microstructure of the alloys, 3A and 3B Keller's reagents were employed. The corresponding micrographs are shown in Fig. 1a–d. As can be seen in Fig. 1a and b, samples HST and HA show well defined grain boundaries together with orientated dark points due to the accumulation of extremely fine $MgZn_2$ precipitates in these zones. Sample HB also show dark points and well defined grain boundaries, but, contrary to the latter alloys, the width of the grain boundary marks are continuous and narrow. The grain boundaries of sample HC appear only after a general attack of the alloy surface (see Fig. 1d), indicating that $MgZn_2$ particles are much more fine and dispersed on the surface than in the case of alloys HST and HA. The observation of all the surfaces attacked by Keller's reagents under the SEM shows, at least in alloys HST and HA, cavities where the $MgZn_2$ precipitates were located. According to actual knowledge of the age-hardening process, an extremely small size of $MgZn_2$ particles is expected for alloys HB and HC [4] and therefore, they are not easily observed. In order to look for differences of the local composition of the alloy surface in the aforementioned cavities, a number of microanalyses of spots (in the range 10–20), inside and outside them were performed. As expected, the total counts corresponding to the elements decreased when the roughness increased. For this reason, the total counts of Al at 1.48 keV, Mg at 1.26 keV and Zn at 1.04 keV, N_{Al}, N_{Mg} and N_{Zn}, respectively, were measured and the ratios $r_{Zn/Al} = N_{Zn}/N_{Al}$, $r_{Zn/Mg} = N_{Zn}/N_{Mg}$ and $r_{Mg/Al} = N_{Mg}/N_{Al}$, calculated, the respective experimental errors being 0.002, 0.060 and 0.002 in all cases. The values corresponding to spots inside and outside the cavities must indicate if there are significant compositional differences between attacked and non-attacked zones. For alloy HST after 20 s etching in 3A Keller's reagent, $r_{Zn/Al}$, $r_{Zn/Mg}$ and $r_{Mg/Al}$ were 0.017, 0.54 and 0.032 inside the cavities and 0.020, 0.60 and 0.034 outside the cavities, respectively. In alloy HC after 30 s etching in 3A Keller's reagent, the ratios were 0.016, 0.66 and 0.024 inside the cavities and 0.018, 0.80 and 0.023 outside the cavities, respectively. These results confirm the Mg and Zn elimination by Keller's etch.

Table 1. Quasistationary corrosion and pitting potentials obtained for Al and Al–Zn–Mg–Cu alloys in 0.1 M NaCl solutions under different experimental conditions, at 25.0 ± 0.1° C.

Sample	Conditions*	E_{cor}† /V(SCE)	E_{Π}‡ /V(SCE)
Al	O_2	−0.69	−0.61
	O_2 + FC	−1.14	−0.62
	Ar	−1.20	−0.62
	Ar + FC	−1.30	−0.60
HST	O_2	−0.86	−0.76 (−0.83)
	O_2 + FC	−0.87	−0.79 (−0.83)
	Ar	−1.00	−0.81 (−0.80)
	Ar + FC	−1.11	−0.81 (−0.82)
HA	O_2	−0.90	−0.76 (−0.83)
	O_2 + FC	−0.89	−0.78 (−0.83)
	Ar	−1.05	−0.83
	Ar + FC	−1.21	−0.84 (−0.83)
HB	O_2	−0.85	−0.77 (−0.81)
	O_2 + FC	−0.84	−0.75 (−0.78)
	Ar	−0.97	(−0.82)
	Ar + FC	−1.11	−0.80 (−0.81)
HC	O_2	−0.80	−0.72 (−0.76)
	O_2 + FC	−0.86	−0.77
	Ar	−1.11	−0.77 (−0.77)
	Ar + FC	−1.20	−0.75 (−0.74)

* O_2: solutions with air dissolved at atmospheric pressure; Ar: solutions deaerated with argon; FC: forced convection using a RDE.
† Quasistationary values measured after 3 h of immersion of samples in solution.
‡ Values in parenthesis are pitting potentials obtained immediately after immersion of samples in solution. For alloys HB and HC, the first pitting potential is reported (see the text).

3.2. *Electrochemical measurements in 0.1 M NaCl*

Electrochemical results obtained for Al and Al–Zn–Mg–Cu alloys are summarized in Table 1. E_{cor} of all samples after immersion in the working solution changed with time from an initial value of about − 1 V (see certain examples in Fig. 2a and b). In air-saturated solutions, E_{cor} changed in the positive direction. However, when after a few minutes a certain potential was reached (e.g. Fig. 2a), it began to oscillate in a range of 10–25 mV around a mean value, which was approximately constant (within ± 20 mV) for an 18 h period. In Fig. 3, a surface micrograph of the alloy HC after 18 h of immersion in an air-saturated 0.1 M NaCl solution is shown, proving pit evolution in certain zones.

In deaerated solutions, E_{cor} changed towards more negative values and quasistationary conditions were approached after a few minutes of the immersion of the alloy. However, continuous and very slow changes in E_{cor} with time were found (see Fig. 2a and b). SEM examination of alloy HA after 3 h of immersion still showed the existence of the precipitates.

Quiescent and forced convection conditions, the latter obtained by means the RDE at 2000 rpm, led to the same quasistationary E_{cor} values in air-saturated solutions except when using high purity aluminium. When electrolyte convection was introduced for high purity aluminium in quasistationary conditions and air-saturated solution, it ceased to oscillate and slowly approached the value obtained for deaerated solutions. Conversely, in the case of deaerated solutions and for all the samples studied, the quasistationary values in quiescent solutions were about 100 mV more positive than those corresponding to electrolytes submitted to a forced convection. Although such quasistationary values were determined up to seven times for each sample, the effect of forced convection in deaerated solutions was proved recording E_{cor} against t with alternacy of quiescent and forced convection conditions (see Fig. 2b). For high purity aluminium and all the alloys studied, whenever electrolyte convection was introduced after reaching the corresponding quasistationary conditions, E_{cor} shifted slowly about 100 mV in the negative direction, and shifted slowly about 100 mV in the positive direction when the forced convection conditions were stopped.

Under quasistationary, deaerated and forced convection conditions, the R_P values at 2 mV s^{-1} were 34 ± 5, 55 ± 5, 75 ± 10 and 105 ± 10 kΩ cm^2 for

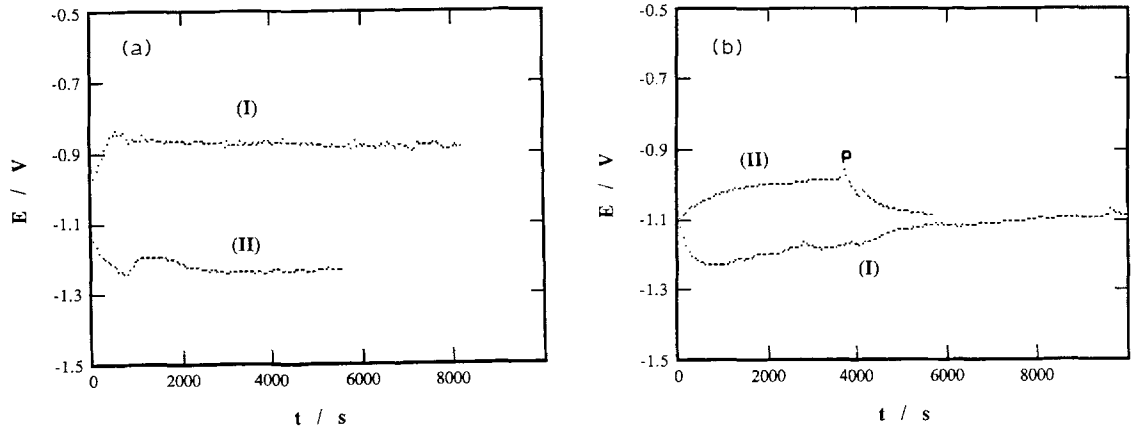

Fig. 2. E_{cor} against time curves in 0.1 M NaCl for different specimens and conditions. (a) Corresponds to alloys HC in (I) air-saturated and quiescent solutions and (II) deaerated and forced convection conditions. (b) Alloy HB in deaerated solutions: (I) under forced convection conditions and (II) performed immediately after curve (I), in quiescent solution, the forced convection being again introduced at point P.

Fig. 3. Pitting corrosion in alloy HC after a 18 h exposure in air-saturated 0.1 M NaCl.

alloys HA, HST, HB and HC, respectively, in front of a value of 135 kΩ cm^2 for high purity Al. In air-saturated solutions, the R_P values for all the alloys were much lower and suffered considerable uncertainty because of the potential oscillation near E_{cor}.

The polarization characteristics of the different samples and conditions studied were compared by means of CPs performed at 1 and 0.2 mV s^{-1} (the sweep rate normally used to obtain the quasistationary *I–E* curves for aluminium in chloride solutions [23]). All the CPs were initiated at the quasistationary E_{cor} measured in deaerated solutions. Several of the experimental curves are presented in Fig 4a and b, in which significant differences in the anodic currents for the different samples employed and the appearance of a maximum (M) only for the alloys HB and HC, can be observed. Such a maximum separates two pitting processes [17–19]. From the CPs, the pitting potentials (E_Π) for alloys HA and HST and the repassivation potentials (E_{RP}) for all the alloys studied were determined by extrapolation of the linear *I–E* regions near the potential of zero current. For alloys HB and HC, E_Π was measured as previously suggested [17–19], i.e. as the extrapolation to zero current of the linear region appearing before the maximum M. Alloy HA was observed under the SEM in the conditions of point P in Fig. 4a, finding a selective corrosion of the $MgZn_2$ precipitates. E_Π and E_{RP} determined for 0.2 and 1 mV s^{-1} coincided within the experimental error (10 mV), although the currents measured were different. It is important to notice that for 0.2 mV s^{-1}, the shoulder T shown in Fig. 4a disappears, the region TL presents higher current and the region TR also present higher current but with greater curvature. Table 1 shows that E_Π of the alloys studied depends on heat treatment and test solution conditions. However, E_{RP} only depends on the heat treatment of the alloy, being of −0.90, −0.88, −0.82 and −0.80 V for alloys HA, HST, HB and HC, respectively. It must be noted that all these E_{RP} values coincide with the corresponding quasistationary E_{cor} in air-saturated solutions.

Anodic Tafel slopes of 24 ± 7 mV dec^{-1} were obtained for all the alloys in air-saturated solutions under quasistationary conditions, independently of convection of the electrolyte. The corresponding cathodic Tafel slopes were very high, the determination of the value being imprecise because of the current oscillation near the pitting potential. Anodic and cathodic Tafel slopes determined in deaerated and forced convection conditions were 0.67 and 0.18 V dec^{-1} for high purity Al, 0.45 and 0.15 V dec^{-1} for alloy HB and 0.44 and 0.13 V dec^{-1} for alloy HST, respectively. For alloy HB and quiescent solutions, the corresponding anodic and cathodic Tafel slopes were 0.51 and 0.16 V dec^{-1}.

Figure 5 shows the aspect of the surface of sample HC after a cyclic polarization between −1.3 and −0.6 V (see curve HC in Fig. 4a). The microanalysis of a spot on the surface of the precipitate indicated the presence of Al, Cl and also very small quantities of Mg and Zn. The CPs were also performed correcting automatically the ohmic drop every 60 s in order to detect the existence of an ohmic control during the process. It must be indicated that the ohmic drop correction was performed automatically by the instrumentation, taking only a time of the order of microseconds to do the operation. As can be seen in Figs. 6 and 7a–f, the attack was then highly enhanced: the anodic charges were much greater and, accordingly, a much higher extent of surface was corroded. However, the pitting potential and the regions more susceptible to the attack were the same as those found when the ohmic drop correction was only performed at the beginning of the experiment. Alloys HST, HA and HB presented the greatest pitting attack in the grain boundaries (see Fig. 7a–c and e). A very different and characteristic

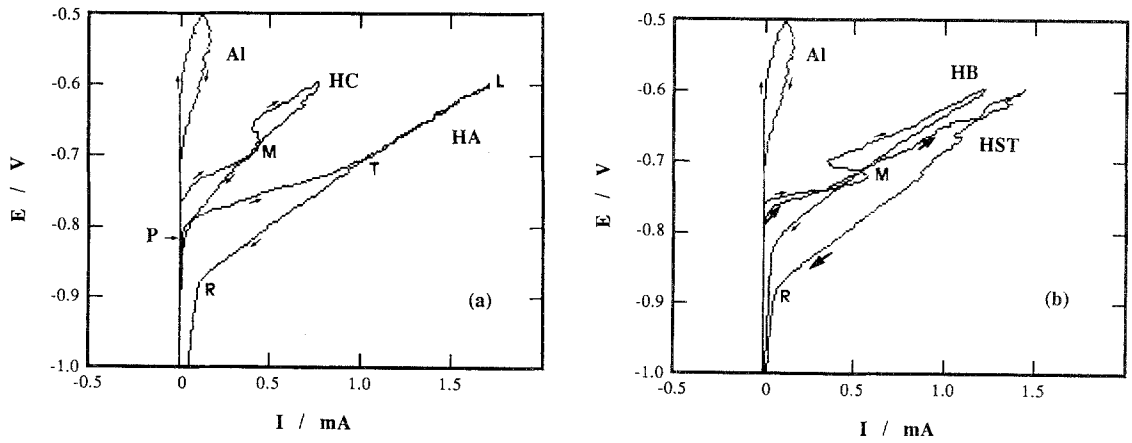

Fig. 4. Cyclic polarization curves at 1 mV s^{-1} for the different specimens in deaerated 0.1 M NaCl solutions. Cross-section of Al: 0.071 cm^2. Cross-section of the alloys: 0.049 cm^2.

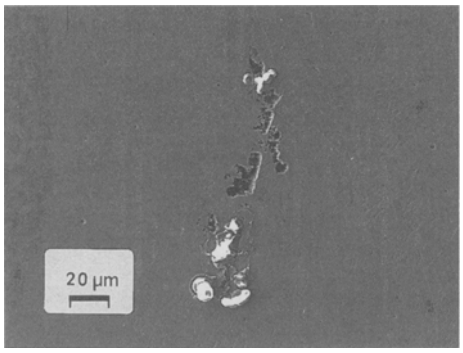

Fig. 5. Surface of alloy HC after the cyclic polarization curve shown in Fig. 4a.

type of attack is evidenced in alloy HC. As shown in Fig. 7f, pitting attack is basically intragranular, the greatest part of the grain boundaries being intact. X-ray mappings of Cl were also performed to know the distribution of the element on the surface of the corroded samples. In Fig. 7d, a representative chlorine X-ray mapping corresponding to the micrograph of Fig. 7c is presented.

In the CP curves with periodical ohmic drop correction, the same trend as those without periodical correction was observed: the total anodic charge for alloys HST and HA was greater than that for alloys HB and HC. The repassivation potentials when such a correction was applied were -1.29, -1.38, -1.15 and -1.14 V for alloys HST, HA, HB and HC, respectively. The latter values approximately coincide with the potential of zero current of the cathodic sweep of the cyclic polarization curves of the corresponding alloys, but are in strong contrast with the values reported in Table 1. For alloy HA the values of the ratios $r_{Zn/Al}$, $r_{Zn/Mg}$ and $r_{Mg/Al}$ inside the pits after the cyclic polarization were 0.013, 0.64 and 0.020 and outside them, 0.019, 0.63 and 0.031, respectively, indicating significant Mg and Zn depletion in the corroded areas.

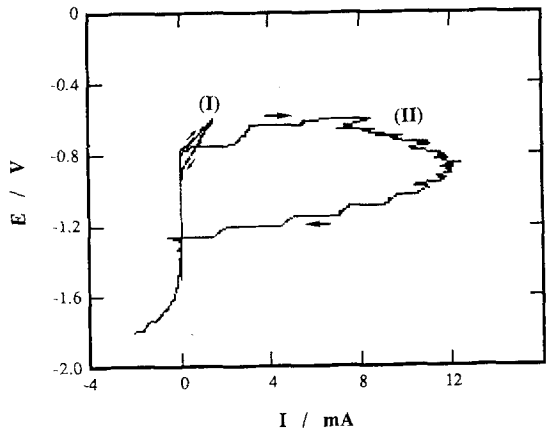

Fig. 6. Cyclic polarization curve corresponding to alloy HST in deaerated and stirred 0.1 M NaCl at 1 mV s^{-1}. (I) ohmic drop correction at the beginning of the experiment, as in the case of Fig. 4 and (II) ohmic drop correction by the current interrupt method every 60 s. Cross-section of the alloy: 0.049 cm^2.

3.3. *Influence of NaCl concentration and Na_2SO_4 addition*

In 0.1 M Na_2SO_4, the E_{cor} against t curves showed the same trend as in 0.1 M NaCl and approximately the same quasistationary potential values were found. However, the E_{cor} oscillation in air-saturated solutions was not detected in 0.1 M Na_2SO_4. The cyclic polarization curves were performed after an immersion time of 4 h and from E_{cor} up to $+2.3$ V. The anodic current for high purity aluminum and all the alloys was in the order of a few microamps in the potential range studied, in strong contrast with chloride containing solutions (cf. Fig. 4a and b). The anodic current slightly increased with potential, but the great rise found in chloride solutions (see Fig. 4a and b) was never detected in the aforementioned potential range for 0.1 M Na_2SO_4. The microscopic observation of the alloy surfaces showed that the anodic dissolution started at points where the localized corrosion developed in NaCl solutions (cf. Fig. 8a and b), that is preferentially in grain boundaries in alloys HA, HST and HB and in the inner part of the grain in alloy HC. However, corrosion further spreads over the surface in 0.1 M Na_2SO_4. On the other hand, the anodic current of the cathodic sweep roughly retraced that of the anodic sweep, principally in alloys HA and HST and, when the experiments were performed under forced convection conditions, the anodic current increased significantly (about one order of magnitude in alloy HA).

E_{cor} values in air-saturated 0.01 M NaCl presented also oscillations of about 30–45 mV around the mean quasistationary value, which were -0.82, -0.80, -0.80 and -0.76 V for alloys HA, HST, HB and HC, respectively. The repassivation potentials, more reproducible than pitting potentials for this concentration, coincided with E_{cor} in air-saturated solutions.

The current increase due to the pit propagation in 0.01 M NaCl–1.0 M Na_2SO_4 appeared at much more positive potentials than those found in the absence of sulphate (see Fig. 9). Figure 10 shows the aspect of the surface of alloy HST after the anodic sweep in which pit propagation took place. Cl and S mappings showed a quite uniform distribution of the elements with high preponderance of the latter. Microanalysis of a spot of the central precipitate in micrograph of Fig. 10 showed a great quantity of Al and S and a small quantity of Zn, Mg and Cl.

Discussion

4.1. *Microstructure of the alloys*

Because of its preparation, alloy HA must have the equilibrium microstructure and therefore, a high concentration of $MgZn_2$ precipitates in the grain boundaries is expected. SEM observation and 3B Keller's reagent attack reveal such a preferential distribution (see Fig. 1b). Apart from the precipitates existing in the grain boundaries, a series of precipitates linearly

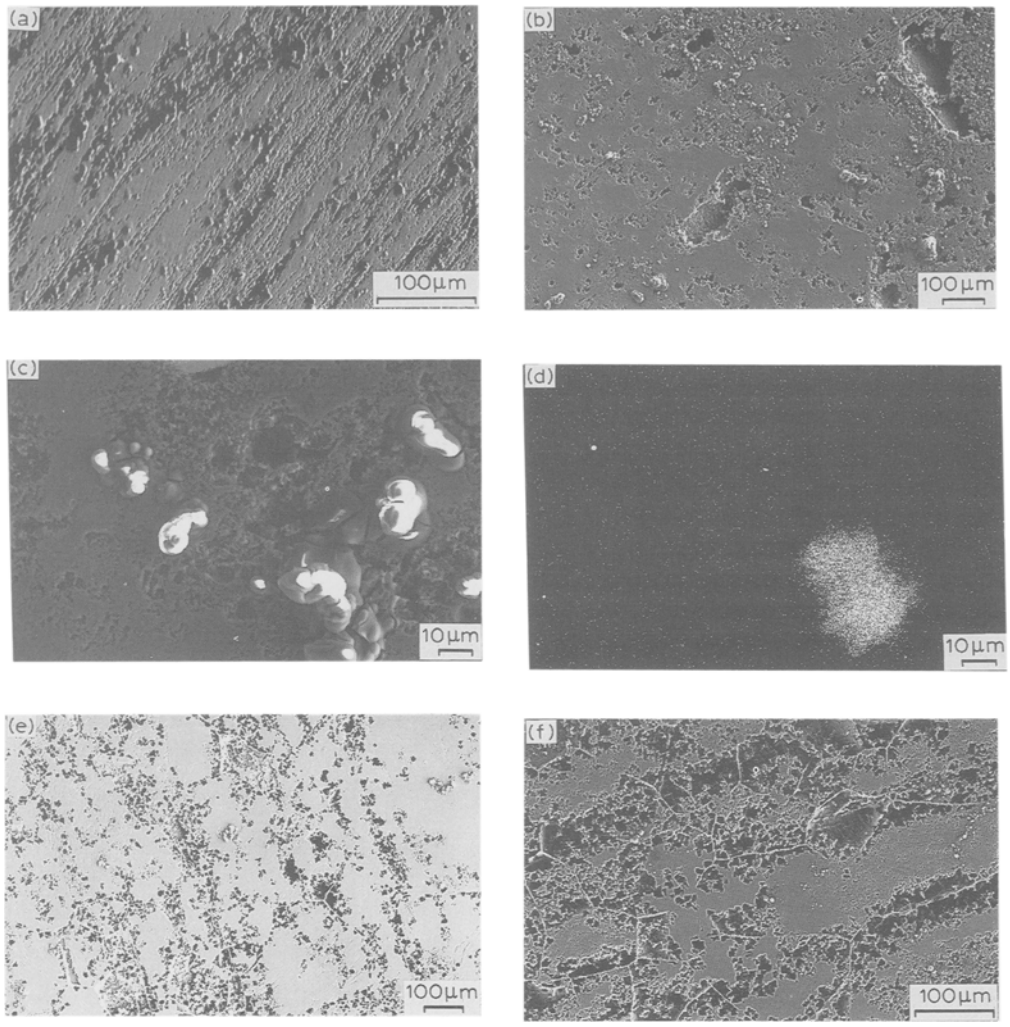

Fig. 7. Surfaces of the alloys after the cyclic polarization at 1 mV s^{-1} in 0.1 M NaCl between −1.2 and −0.6 V with ohmic drop correction by the current interrupt method every 60 s. (a) Alloy HST; (b) alloys HA; (c) and (d) detail of alloy HA and the corresponding Cl mapping; (e) alloy HB; and (f) alloy HC.

distributed in the grains are also observed. Alloy HST presents a composition near to that of the equilibrium, but its grain structure differs from that of alloy HA. Alloy HST shows enlarged and deformed grains because of the cold rolling, the direction of the grains corresponding to the effort applied (see Fig. 1a).

According to 3B Keller's etching, extremely fine $MgZn_2$ precipitates can be expected in the grain boundaries and in the inner part of the grains of alloy HB (see Fig. 1c). The precipitates appear to be much more fine and dispersed than in the case of alloys HST and HA. This result can be easily explained from the known metallurgical changes produced by its heat treatment sequence [20, 25], the following microstructure being expected: Guinier-Preston (GP) zones, Zn and Mg grain boundary segregation, small quantity of

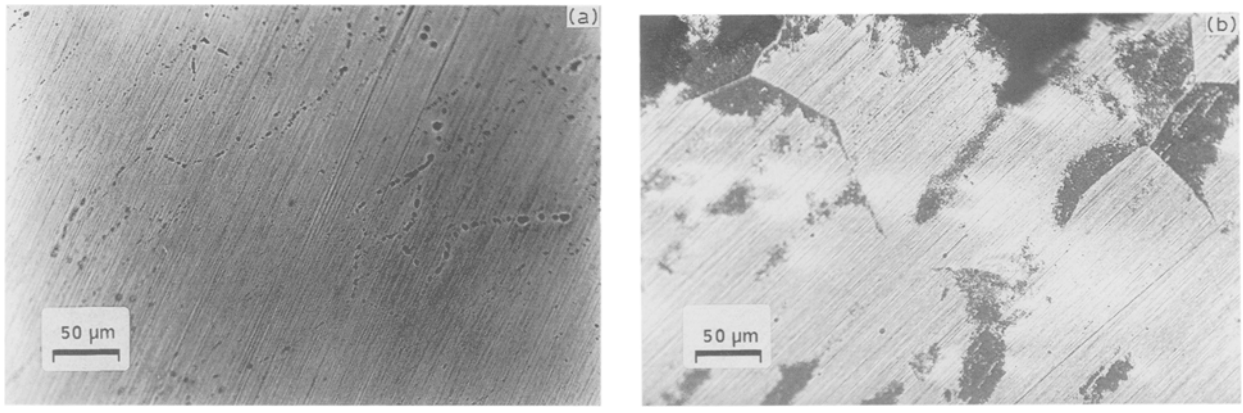

Fig. 8. Surface attack of the alloys after potentiodynamic polarization in 0.1 M Na_2SO_4. (a) Alloy HA stopping the anodic sweep at 1.6 V, in quiescent and air-saturated solution and (b) alloy HB after cyclic polarization between −1.2 and +2.2 V in air-saturated and stirred solution. Potentials referred to saturated Hg/Hg_2SO_4 reference electrode.

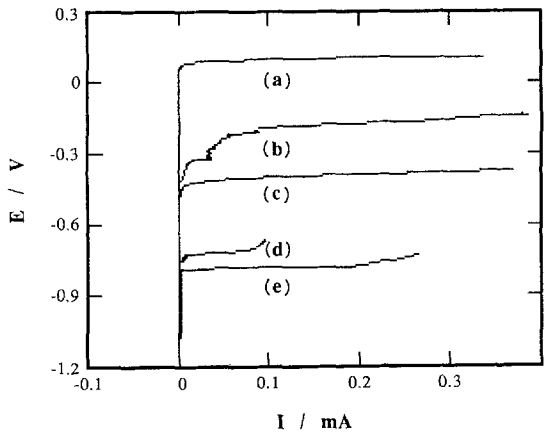

Fig. 9. Potentiodynamic polarization curves of the alloys at $1\,mV\,s^{-1}$: (a), (b) and (c) alloys HB, HST and HA, respectively, in deaerated quiescent 0.01 M NaCl–1.0 M Na_2SO_4 solution; (c) and (d) alloys HC and HST, respectively, in air-saturated quiescent 0.01 M NaCl after 3 h of sample immersion. Cross-section of the alloys: $0.049\,cm^2$.

$MgZn_2$ precipitates in the inner part of the grain and a higher extent of $MgZn_2$ precipitates in the grain boundaries. The existence of Zn and Mg segregation can be explained by the vacancy drag mechanism, a non-equilibrium segregation model which supposes that solute atoms are pumped to the grain boundaries depending on the grain size and on the quenching rate [24, 26, 27]. According to the literature [28, 32], the number of vacancies increase with the temperature. At high temperatures, the proportion of free vacancies is much greater than those complexed with solute atoms. However, as the temperature decreases, the proportion of combined vacancies increase in such a form that is greater than those free. As long as such vacancies are absorbed by the grain boundaries in the cooling process, solute atoms are pumped to the grain boundaries. In the ageing process and depending on the concentration distribution gradient of Zn and Mg, part of the Mg atoms reacts with Zn to form $MgZn_2$. The non-combined Mg remains in free form in the grain boundaries [25, 33–35], appearing to be responsible for the SCC of the alloy [26, 36–38]. It is possible to calculate, approximately, the thickness of the free precipitate zone near the grain boundaries as a function of the quenching rate [39, 40]. In the case of alloy HB, such a thickness is estimated to be about $4\,\mu m$, which is much lower than the mean grain size of $225 \pm 40\,\mu m$. Therefore, 3B Keller's reagent shows the grain boundaries where $MgZn_2$ precipitates and a Mg enrichment exist, but the free precipitate zone is not revealed (see Fig. 1c).

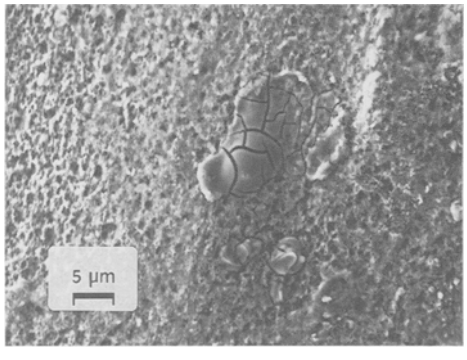

Fig. 10. Surface of alloy HST after a potentiodynamic polarization between −1.2 and 0.2 V in deaerated and quiescent 0.01 M NaCl–1.0 M Na_2SO_4, the ohmic drop correction being performed by the current interrupt method every 60 s.

Although the mean grain size in alloys HA, HB and HC appears to be the same, the distribution of precipitates is very different. In alloy HC, the dispersion of GP zones and precipitates in the inner part of the grain appears to be similar to that of alloy HB, but great differences in the composition of the grain boundaries are evidenced. According to Gárlipp *et al.* [21], the breaking strains of non-corroded HB and HC alloys were 454 ± 8 and $435 \pm 2\,MN\,m^{-2}$, respectively, whereas for the same alloys corroded in $3\,g\,dm^{-3}$ NaCl + $36\,g\,cm^{-3}$ CrO_3 + $30\,g\,cm^{-3}$ $K_2Cr_2O_7$ boiling solution for 3.5 h, they were of 306 + 32 and $417 \pm 20\,MN\,m^{-2}$, respectively, i.e. $67(\pm 8)\%$ and $96(\pm 5)\%$ of the values corresponding to the non-corroded samples. The fracture of the corroded alloy HB exhibited a mixing of grains non-deformed together with other ones with plastic deformation, while in the case of alloy HC, only plastically deformed grains were observed. All these results can also be explained by the vacancy drag model, because when the quenching process is interrupted at a temperature where the great part of the vacancies are not combined with solute atoms, many of such vacancies can be absorbed by the grain boundaries without dragging solute atoms [21]. The quantity of solute atoms dragged to the grain boundaries in alloy HC was much lower than for alloy HB because of the interrupted quenching process and hence, much smaller quantities of $MgZn_2$ precipitates and free Mg in the grain boundaries are expected.

4.2. *Electrochemical behaviour in 0.1 M NaCl*

The anodic and cathodic Tafel slopes indicate that the cathodic reaction is highly polarized in air-saturated 0.1 M NaCl and hence, cathodic control is inferred under such conditions. Conversely, the anodic process governs the total reaction in the deaerated solution. On the other hand, the R_p values determined in air-saturated solutions are much lower than those found in deaerated solutions, indicating higher corrosion rates in the former. These results, as well as the evidence in Fig. 3, allow the quasistationary values measured in air-saturated solutions to be ascribed to pitting evolution and the potential oscillation to the instability of the system which undergoes pitting. Polarization by dissolved oxygen up to the pitting potential has also been reported for different aluminum alloys [3].

The equilibrium potential of the electrode $Al_2O_3 \cdot 3H_2O/Al$ is calculated to be −2.275 V at pH 7, this indicating that in the E_{cor} conditions reported in Table 1 for deaerated and air-saturated solutions, aluminum should be protected by a passivating oxide layer. Therefore, in deaerated solutions, the metal

corrosion must take place in the form of passive corrosion, the anodic process leading to the oxide formation and the cathodic process being the reduction of water. However, in air-saturated solutions, oxygen is the reducible species and the anodic reaction corresponds to pit evolution.

The Tafel slopes for hydrogen evolution on aluminium and on many other metals are about 0.12 V dec^{-1} (without surface oxide or at least, in the case of aluminium with the minimum residual oxide) [41–43], which is a value lower than those obtained in the present work. Values of cathodic Tafel slopes greater than 0.12 V dec^{-1} can be ascribed to the presence of an oxide film on aluminum, as previously demonstrated [44]. In addition, Moshier *et al.* [45] have shown by means of XPS that an oxyhydroxide phase close to boehmite, AlOOH, is formed on aluminum after about 1 h of immersion in neutral solutions, which changes to gibbsite, $Al(OH)_3$, after 10–20 h of exposure.

The values of R_P, E_{cor} and Tafel slopes obtained in the present work can be interpreted according to the breakdown and repair theory of the oxide films on metals [46]. Whenever the active metal area increases due to the film breakdown, E_{cor} shifts in the negative direction and the corrosion current increases. On the contrary, when the metal is repassivated, E_{cor} shifts in the positive direction and the corrosion current decreases. This explains that for deaerated solutions, E_{cor} decreases just after the immersion of the sample and under forced convection conditions, they become more negative than those of quiescent solutions. It must be accepted that the oxyhydroxide film formed on aluminum and its alloys presents flaws or defects through which the anodic or cathodic processes can take place, because if such an oxide were completely uniform and passivating, no E_{cor} changes would be found when introducing the forced convection. As a consequence, the E_{cor} decrease in deaerated solutions is ascribed to an increase in the anodic area because forced convection favours the removal of the oxidation products from the alloy surface.

In free corrosion conditions of high-purity aluminium in air-saturated 0.1 M NaCl, the metal under the defects or flaws of the initial oxide film is oxidized to form new oxide which can further grow and therefore, E_{cor} shifts in the positive direction. The formation of new oxide in the presence of chloride permits to develop local conditions favouring pit nucleation and further pit propagation. When forced convection is introduced, local conditions previously created can be disturbed and then, the active area increases, E_{cor} shifts in the negative direction and pitting corrosion ceases.

A similar interpretation can be performed for the alloys studied, although the question related to the role of dissolved Zn, Mg and Cu and $MgZn_2$ precipitates must be considered. A pitting potential of -1.1 V was reported for the latter compound in deaerated 1 M NaCl and a maximum difference of 100 mV is estimated when changing the NaCl concentration from 1 to 0.1 M [47]. On the other hand, a small quantity of copper appears to be incorporated in the $MgZn_2$ phase, as indicated by the corresponding spot microanalysis. Copper incorporation in this phase, as Mg (Al, Cu, $Zn)_2$, has been previously described for overaged 7075 Al–Zn–Mg alloy [18] and this probably modifies the breakdown potential of the $MgZn_2$ phase in the positive direction.

The anodic Tafel slopes for the alloys in deaerated solutions are lower than the value corresponding to high-purity aluminium and the R_P values decrease in the order Al, HC, HB, HST and HA. The E_{cor} about -1 V measured for the alloys in quiescent and deaerated solutions and the negative shift when forced convection is introduced, can also be explained by the breakdown and repair theory of oxide films, the passive corrosion being anodically-controlled. The R_P values indicate that the oxide film on the alloys presents more flaws and defects than for high purity aluminium, with the corresponding increase of the corrosion rate. This is not surprising because the resistance to corrosion of high purity aluminium is due to aluminum oxide and the alloys present elements of a quite different nature.

As shown in Fig. 4a and b, alloys HB and HC present two pitting potentials while high purity aluminium and alloys HA and HST exhibit only one pitting potential. The E_{Π} data obtained in deaerated solutions (see Table 1) indicate a decrease in the susceptibility to pitting attack following the order HA, HST, HB, HC and Al. The pitting potentials of aluminium alloys are associated to the phases or regions of different composition present in the alloy and are electrochemically detected when such regions or phases exist in a sufficient quantity [3, 17, 18]. This makes it possible to recognize two different zones susceptible to pitting attack in alloys HB and HC. When considering the very small size and high dispersion of the $MgZn_2$ precipitates in alloys HB and HC and the previous discussion on the pitting potential of $MgZn_2$, it is highly improbable that one of the pitting potentials corresponds to the attack of this latter phase. On the other hand, Fig. 7e shows pitting attack in the matrix and also intergranular and therefore, alloy HB is susceptible to SCC, in agreement with previous loading tests [21]. As pointed out above, a Mg and Zn enriched region is localized close to the grain boundaries and as long as such elements make the alloy more anodic, the grain boundaries will be the first region to be attacked during the anodic sweep. At more positive potentials, pitting of the matrix also takes place. A similar situation has been described by Maitra and English [18] using an Al–Zn–Mg alloy with higher contents in Zn, Mg and Cu but also cold water quenched and artificially aged. Alloy HC, although two pitting potentials were also observed at potentials similar to those found for alloy HB, did not suffer intergranular attack after the cyclic polarization assay (see Fig. 7f). This indicates that alloy HC is more resistant to SCC, in agreement with previous loading tests [21]. When comparing the behavior of alloys HB and HC, it must be concluded that the two

zones of different composition in alloy HB are distributed in a different form in alloy HC. According to the microstructural results, the Mg and Zn enriched region in alloy HC is also parallel but situated at greater distance from the grain boundaries than alloy HB.

The interest of studying alloys HA and HST was for correlating the $MgZn_2$ precipitates with localized attack of the samples. E_{Π} values for alloys HST and HA are more negative than those for alloys HB and HC and only one pitting potential is found. Although pitting attack took place near to the $MgZn_2$ precipitates, pitting of the matrix is clearly revealed after the cyclic polarization (see Fig 7a and b). The matrix of alloy HA and HST surely has a lower content in copper than the matrix of alloys HB and HC, as indicated by the microanalysis of spots of $MgZn_2$ precipitates in alloy HA. However, the change of the solution potential of the alloy when copper concentration is changed from zero to 0.5% is only of about 4 mV [3] and the total composition of copper in the present alloys is 0.23%. On the other hand, the Zn and Mg contents of the matrix of alloys HA and HST are expected to be lower than in the case of alloys HB and HC, because the latter have metastable supersaturated phases produced by cold water quenching. The microscopic observation of alloy HA at point P, that is before pit propagation, shows selective corrosion of $MgZn_2$ and, in addition, a significant current which slowly decreases is found after the linear region of the cathodic sweep (i.e. after point R in Fig. 4a and b). Therefore, it is concluded that $MgZn_2$ precipitates play an important role in the pitting corrosion behaviour of alloys HA and HST. Finding a typical pitting corrosion behaviour in small and highly dispersed precipitates is improbable because they are not continuous. However, they may act as pit nucleation centers. With the current focusing in the $MgZn_2$ which are being dissolved, a higher local chloride concentration is produced in the resulting cavities. The local conditions favour pit propagation in the matrix near such precipitates. It is well known that pit growth is an autocatalytic phenomenon, the composition of the pits being different from that of the bulk solution [23]. Pit propagation undoubtedly discovers new $MgZn_2$ precipitates following the grain boundaries or even in the inner part of the grain and as a greater quantity of such precipitates are localized in the grain boundaries, pits propagate preferentially in the intergranular direction. Although the cathodic sweep retraces the region TL of the anodic sweep (see Fig. 4a), the region TR reveals the influence of a greater quantity of $MgZn_2$ phase, because pitting corrosion has been extended in the intergranular regions, permitting easily the pit propagation in these zones.

Results of Table 1 indicate a certain effect of dissolved oxygen in the CP curves. For all the alloys, E_{Π} values are independent of convection, presence of oxygen and immersion time in the solution, except when the samples are immersed in air-saturated solutions for long times. In this case, E_{Π} is more positive, whereas E_{RP} values do not depend on convection, presence of oxygen and immersion time in the solution. Since the alloys undergo pitting corrosion in aerated solutions, it is interpreted that the prolonged action of oxygen is the elimination of part of the most anodic phase, pit nucleation than being more difficult.

It is also observed in Figs. 5 and 7a–f that the greatest part of the attacked zone appears covered by an aluminium chloride precipitate of the same characteristics, independently of the application of the periodical current interrupt *IR* compensation. This indicates that such precipitates are not an artifact of the latter correction. Moreover, chloride is not present in significant quantities in those zones where the precipitates are not found. The appearance of these precipitates is not crystalline and when dryed under Ar stream and high vacuum, they are broken forming crevices. On the other hand, not all the precipitates show a significant quantity of aluminium chloride. This indicates that part of the aluminium oxidation leads to the formation of oxide, probably hydrated. When the pit is active, such a film permits chloride penetration and pit propagation, while when the oxide film formation predominates on chloride attack, the pit becomes passive and the existence of chloride is practically not detected. These results are easily interpreted when considering that pit propagation takes place under ohmic control. The current densities at -600 mV for the alloys studied are of the order of a few mA cm^{-2}, this implying high current densities in localized points. As pit propagation develops in the active pits, which are covered by a layer composed by aluminium oxide and chloride, the ohmic control in the pitting corrosion process must correspond to ion migration through such layers. As the main electrochemical process takes place in the active pits, this indicates that they are covered by a layer more conductive than the oxide layer covering the regions which have not suffered attack. When the ohmic drop is corrected every 60 s, the resistance of the layer covering the pits is compensated and a new potential is applied favouring pit propagation in the more susceptible areas.

4.3. *NaCl concentration and Na_2SO_4 addition effects*

As shown by the experimental results, sulphate ions are responsible for a general corrosion of the alloys. Such a corrosion starts at points where the oxide is less protective, that is in the grain boundaries in alloys HA, HST, HB and in the inner part of the grain in alloy HC, as found in chloride solutions. However, further oxidation spreads the attack over the surface and no pitting attack is found in the potential range studied. The anodic current densities measured are of the order of magnitude of those corresponding to oxide film formation by ionic conduction, although they are higher than the stationary current densities of 2 μA cm^{-2} at 1 mV s^{-1} measured in H_3BO_3-borax solution, an electrolyte which permits oxide formation with high efficiency [48]. Therefore, the efficiency for

the oxide formation on the alloys studied in sulphate solutions appears to be low.

As can be deduced from Figs. 9 and 10, the effect of combined additions of chloride and sulphate produces general corrosion of the sample and pitting attack in certain areas. The most remarkable feature is that sulphate considerably shifts the pitting potential in the positive direction (see Fig. 9). In the microscopic examination of the alloys polarized up to pit propagation, many precipitates of the type appearing in Fig. 10 were observed all over the corroded surface. Such precipitates are typical of pitting attack by chloride ion (see Figs. 3, 5, 7a–c) and then, they are related to the current increase shown in Fig. 9. The shift in the pitting potential can be explained by the fact that both sulphate and chloride are competitively adsorbed on the oxide film. As long as there is a great proportion of sulphate, it is very difficult for chloride ion to be adsorbed and build up local conditions with sufficient concentration to develop pitting attack.

5. Conclusions

The electrochemical study of the corrosion behaviour of Al–(5.03%)Zn–(1.67%)Mg–(0.23%)Cu, submitted to heat treatments of annealing (HA), cold rolling (HST), cold water quenching and ageing (HB) and interrupted quenching and ageing (HC), in chloride and sulphate solutions, under deaerated and air-saturated conditions have led to the following conclusions:

1. The passive corrosion of the samples studied in deaerated solutions decreases in the order HA, HST, HB, HC and Al. Corrosion of the alloys in such conditions are attributed mainly to deffective oxide on Zn and Mg enriched regions and on $MgZn_2$ precipitates.
2. Free corrosion potentials in air-saturated solutions present oscillations of a few tens of mV around a quasistationary mean value, which sensibly coincides with the repassivation potential of the samples.
3. Susceptibility to pitting attack decreases in the order HA, HST, HB, HC and Al. High purity Al and alloys HA and HST present a single pitting behaviour, the process being initiated in the $MgZn_2$ enriched regions, which activate pitting of the matrix. Alloys HB and HC exhibit two pitting processes: the first one, at more negative potentials, in the Mg and Zn enriched regions and the second one, in the matrix.
4. Alloys HA and HST are susceptible to intergranular attack because of the greater quantity of $MgZn_2$ in the grain boundaries. The age hardened alloy HB is susceptible to intergranular corrosion and therefore to the SCC, because the Mg and Zn enriched regions are situated in the grain boundaries. Alloy HC is more resistant to SCC, because the Mg and Zn enriched regions are probably situated parallel but at a certain distance of the grain boundaries.
5. Pit propagation takes place under ohmic control, probably by ion migration through a layer composed by hydrated aluminum chloride and oxide. Ohmic drop correction by the current interrupt method highly enhances pitting corrosion, showing clearly the regions of the alloy more susceptible to pitting attack.
6. Sulphate ions promote general corrosion of the alloys. However, the corrosion starts in the Mg and Zn enriched regions and in the $MgZn_2$ phase. The presence of sulphate in the chloride solutions considerably shifts the pitting potential towards the positive direction, because the sulphate adsorption on the alloy precludes chloride accumulation and further pit nucleation at localized points.

Acknowledgements

The authors gratefully acknowledge financial support of this work by the Dirección General de Investigación Científica y Técnica (DGICYT, Spain) under project PB87-0179. Financial support for the scientific exchange by the Conselho Nacional de Pesquisas (CNPq, Brazil) and the Consejo Superior de Investigaciones Científicas (CSIC, Spain) is also acknowledged. The authors also thank the Servei Científico-Tècnic de la Universitat de Barcelona (Univ. de Barcelona, Spain) for the facilities in the SEM observations and Dr S. R. Fontarnau, W. Gárlipp, M. Cilense and J. B. Bessone for useful discussions.

References

[1] G. Eger, *Intern. Z. Metallog.* **4** (1913) 29.
[2] W. Sander and K. L. Meissner, *Z. Anorg. Allgem. Chem.* **154** (1926) 144.
[3] 'Corrosion', *in* 'Metals Handbook', 9th ed., Vol. 13; Am. Soc. for Metals, Metals Park, Ohio (1987) pp. 583–609.
[4] L. F. Mondolfo, *Metall. Rev.* **16** (1971) 95.
[5] Y. Baba, *J. Jpn. Inst. Met.* **31** (1967) 507.
[6] Y. Baba, *Trans. Him.* **11** (1970) 104.
[7] W. F. Smith and N. J. Grant, *Metall. Trans. A* **2** (1971) 1333.
[8] H. Cordier, C. Dumont and W. Gruhi, *Metall.* **32** (1982) 33.
[9] I. J. Polmear, *J. Inst. Met.* **87** (1958–59) 65.
[10] G. Thomas and J. Nutting, *J. Inst. Met.* **88** (1959–60) 81.
[11] I. J. Polmear, *J. Inst. Met.* **89** (1960–61) 51.
[12] E. H. Dix, *Trans. Am. Soc. Metals* **42** (1950) 1057.
[13] H. A. Holl, *J. Inst. Met.* **97** (1969) 200.
[14] W. Gruhi and H. Cordier, *Aluminium* **44** (1968) 403.
[15] H. Cordier, C. Dumont and W. Gruhi, *ibid.* **55** (1979) 777.
[16] *Idem. Metall.* **34** (1980) 315.
[17] J. R. Galvele and S. M. de Micheli, *Corros, Sci* **10** (1970) 795.
[18] S. Maitra and G. C. English, *Metall. Trans.* **12A** (1981) 535.
[19] S. C. Byrne, *in* 'Aluminum Alloys, Physical and Mechanical Properties', Vol. II, (edited by E. A. Stark and T. H. Sanders), Warley, UK (1986) pp. 1095–107.
[20] G. M. Scamans, N. J. H. Holroyd and C. D. Tuck, *Corros. Sci.* **27** (1987) 329.
[21] W. Gárlipp, S. Saimoto and H. M. dos Santos, Proceedings of the Meeting of the Associação Brasileira de Metais, Belo Horizonte, M. G., Brazil (1987) pp. 33–44.
[22] Metallography and Microstructures *in* 'Metals Handbook', 9th ed., Vol. 9 Am. Soc. for Metals, Metals Park, Ohio (1985) pp. 351–60.
[23] H. Kaesche, *Werkt. Korros.* **39** (1988) 152.
[24] S. L. Cundy, A. J. F. Metherrel, M. J. Whelan, P. N. T. Unwin and R. B. Nicholson, *Proc. R. Soc. Lond. A* **307** (1968) 267.
[25] J. M. Chen, T. S. Sun, R. K. Viswanadham and J. A. S. Green, *Met. Trans.* **8A** (1977) 1935.
[26] R. K. Viswanadham, T. S. Sun and J. A. S. Green, *Met. Trans.* **11A** (1980) 85.
[27] T. R. Anthony, *Acta Metall.* **17** (1969) 603.
[28] R. E. Howard and A. B. Lidiard, *Phil. Mag.* **12** (1965) 1179.
[29] A. Ascoli, G. Guarini and G. T. Queirolo, *Crystal Lattice Defects* **1** (1970) 159.
[30] A. Ascoli, P. Bergamini and G. T. Queirolo, *Scr. Metall.* **6** (1972) 641.

[31] Th. Hehenkamp and L. Sander, *Z. Metallkd.* **70** (1979) 202.
[32] F. Faupel and Th. Hehenkamp, *Scr. Metall.* **18** (1984) 597.
[33] P. Doig and J. W. Edington, *Br. Corros. J.* **9** (1974) 220.
[34] *Idem., Br. Corros. J.* **9** (1974) 461.
[35] *Idem., Metall. Trans.* **6A** (1975) 943.
[36] R. J. Gest and A. R. Troiano, *Corrosion* **30** (1974) 274.
[37] G. M. Scamans, R. Alani and P. R. Swann, *Corros. Sci.* **16** (1976) 443.
[38] R. Alani and P. R. Swann, *Br. Corros. J.* **12** (1977) 80.
[39] J. D. Embury and R. B. Nicholson, *Acta Metall.* **13** (1965) 403.
[40] S. Chang and J. E. Morral, *Acta Metall.* **23** (1975) 685.
[41] A. K. Vijh, *J. Phys. Chem.* **72** (1968) 1148.
[42] P. L. Cabot, F. Centellas, J. A. Garrido, E. Pérez and H. Vidal, *Electrochim. Acta* **36** (1991) 179.
[43] J. M. Costa, *in* 'Fundamentos de Electródica', Alhambra, Madrid (1981) p. 221.
[44] A. K. Vijh, *J. Phys. Chem.* **73** (1969) 506.
[45] W. C. Moshier, G. D. Davis and J. S. Ahearn, *Corros. Sci.* **27** (1987) 785.
[46] J. M. West, *in* 'Electrodeposition and Corrosion Processes', Van Nostrand, London (1965) pp. 86–93.
[47] H. Böhni and H. H. Uhlig, *J. Electrochem. Soc.* **116** (1969) 906.
[48] P. L. Cabot, F. Centellas, J. A. Garrido and E. Pérez, *J. Appl. Electrochem.* **17** (1987) 104.